

Nitrogen-Doped Carbon-Coated 2D Cobalt Phosphide Nanosheets for High-Performance Sodium Storage

Jingyu Guo, Qingzhe Meng, Kaizhong Li, Jiahao Cai, Zhan Zhao, Jinheng Wang, Yang Li, Xiangjuan Zhao, Mingyao Xu, Yunxiu Wang, Xiaomei Song, Zhongchao Bai,* and Caifu Dong*

A rational structural design is an effective way to enhance the sodium storage cycle stability and reaction kinetics of metal phosphides. Therefore, nitrogen-doped carbon-coated CoP nanosheets are obtained by a facile solvothermal method coupled with a polydopamine coating and phosphorization strategy. Combining the advantages of the nitrogen-doped carbon layer and the nanosheet structure, the pseudocapacitance contribution and reaction kinetics of CoP@NC are significantly enhanced compared to pure phase CoP, as evidenced by electrochemical tests

including cyclic voltammetry and GITT. Based on this, CoP@NC exhibits excellent cycling stability and rate performance. A specific capacity of 169 mAh g^{-1} can be maintained after 100 cycles at a current density of 0.5 A g^{-1} , corresponding to a capacity drop of only 0.2% per cycle. In addition, the CoP@NC electrode can deliver the discharge capacities of up to 303.3 and 106.6 mAh g^{-1} at 0.1 and 2 A g^{-1} , respectively. These excellent properties demonstrate that CoP@NC is a promising anode material for sodium storage.

1. Introduction

Sodium ion batteries (SIBs) are considered a reliable alternative to lithium-ion batteries due to sodium's abundant resources, wide distribution, and similar properties to lithium.^[1–3] However, the radius of the sodium ion is 1.5 times larger than that of the lithium ion, which requires a more robust electrode material in terms of both structure and electrochemical kinetics.^[4,5] For example, commercial graphite can exhibit a specific capacity of 372 mAh g^{-1} when used as a lithium anode. However, it has almost no capacity (35 mAh g^{-1}) when used as an anode for SIBs.^[6,7] Therefore, the negative electrode

material needs to be properly selected and designed to match the high-capacity positive electrode material.

Among the various anode materials for SIBs, conversion-type metallic phosphides (TMPs; M = Fe, Ni, Mo, and Co.) have attracted a lot of attention because of their lower polarization ($\approx 0.4 \text{ V}$) compared to fluorides ($\approx 1.1 \text{ V}$), oxides ($\approx 0.9 \text{ V}$) and sulfides ($\approx 0.7 \text{ V}$), which are more suitable for ion storage.^[8,9] In particular, CoP is an ideal choice as an anode material for SIBs because of its high theoretical specific capacity of 894 mAh g^{-1} and its high activity and low cost.^[10] However, the electrical conductivity of CoP remains poor and the electrochemical reaction still produces large volume changes, which have serious implications in terms of rate performance and cycling stability.^[11,12] Constructing composites of metal phosphide nanosheets with carbon can effectively alleviate the above problems. Such composites have the following advantages:^[13–15] 1) it can increase the contact area between the electrode material and the electrolyte, shortening the ion transport distance; 2) it can reduce the charge transfer impedance to improve the reaction kinetics, and 3) it can alleviate the volume change during the electrochemical process to enhance the cycling stability of the electrode material. For example, Yin et al. coated Cu₃P nanosheets into the carbon layer to form Cu₃P@P/NC, which showed significantly improved sodium storage properties compared to pure phase Cu₃P.^[16] In addition, hierarchical Ni₂P nanosheets/three-dimensional graphene (3DG), composite synthesized by Wu et al., also showed higher sodium storage properties than pure Ni₂P.^[17] Despite this, very few studies have been conducted on the sodium storage properties of carbon-coated CoP nanosheet composites.

Herein, we precisely synthesized nitrogen-doped carbon-coated CoP nanosheets (CoP@NC) and pure CoP nanosheets. Compared to pure CoP, CoP@NC electrodes exhibit higher

J. Guo, Q. Meng, K. Li, J. Cai, Z. Zhao, J. Wang, Y. Li, X. Zhao, M. Xu, Y. Wang, C. Dong

School of Environmental and Material Engineering, and Trier College of Sustainable Technology

Yantai University

Yantai 264005, P. R. China

E-mail: dongcf@ytu.edu.cn

Y. Wang, X. Song

Yantai Key Laboratory of Fine Chemical Wastewater Treatment and Recycling (Preparatory)

Yantai 264005, P. R. China

X. Song

Shandong (Yantai) Sino-Japan Industrial Technology Research Institute (Yantai Industrial Technology Research Institute)

Yantai 264005, P. R. China

Z. Bai

Institute of Energy Materials Science

University of Shanghai for Science and Technology

Shanghai 200093, P. R. China

E-mail: baizhongchao@tyut.edu.cn



Supporting information for this article is available on the WWW under <https://doi.org/10.1002/batt.202500625>

reversible capacity, cycling stability, and rate capability when used as anodes for SIBs. In particular, it delivers a reversible capacity of 147 mAh g^{-1} at 0.5 A g^{-1} for over 200 cycles. Furthermore, it shows excellent rate performance (303.3 mAh g^{-1} at 0.1 A g^{-1} and 106.6 mAh g^{-1} at 2 A g^{-1}) for sodium storage. The enhanced electrochemical performance of CoP@NC compared to pure phase CoP can be attributed to the improved reaction kinetics and the contribution of pseudocapacitance as demonstrated by cyclic voltammetry (CV) and GITT tests.

2. Results and Discussion

Figure 1a shows a schematic illustration of the synthesis of CoP@NC. First, the metal ions self-assemble with mln to form smooth polygonal nanosheet precursors during the solvothermal reaction. The thickness of the precursor varies between 400 and 600 nm (Figure S2, Supporting Information). Then, CoP nanosheets with rough surfaces are obtained by phosphorylating the precursors. Finally, CoP@NC was obtained by coating the CoP nanosheets with PDA followed by carbonization. Figure 1b shows the field-emission scanning electron microscopy (FESEM) image of the precursor, from which it can be seen that the precursor is a smooth polygonal nanosheet. According to Figure 1c,d, the nanosheet structure can be maintained after the vapor-phase phosphorization process, but the surface becomes rough. Figure 1e and Figure S1, Supporting Information, show the transmission electron microscopy (TEM) and FESEM images of CoP@NC, respectively, showing that the target material also maintains the nanosheet structure, but with a rougher surface, which is probably due to the coating of the

carbon layer on the surface. The uniform distribution of Co, P, C, and N can be seen in the FESEM (Figure 1f) and the corresponding elemental mapping.

The crystallographic structure of the CoP and CoP@NC is investigated by X-ray diffraction (XRD). As shown in **Figure 2a**, the diffraction peaks at 31.6° , 36.3° , 46.2° , 48.1° , and 56.8° correspond to the (011), (111), (112), (211), and (301) planes of CoP (JCPDS card no. 01-089-4862). No characteristic peaks of carbon were detected in the XRD pattern of CoP@NC, which may be attributed to the amorphous nature of carbon. To confirm the presence of carbon, Raman spectra of CoP and CoP@NC were tested. In the Raman spectrum of CoP@NC, the D and G peaks of carbon were detected, and the ID/IG was calculated to be about 0.88, indicating the presence of defective carbon in CoP@NC, which facilitates the transport of electrons. Additionally, the carbon layer can mitigate volume expansion during the electrochemical process, leading to superior performance. The specific surface area (Figure 2c), BJH pore size distribution (Figure 2d), and pore volume of CoP@NC are analyzed by N_2 adsorption-desorption isotherms. The results showed that the specific surface area of CoP@NC is $127.8 \text{ m}^2 \text{ g}^{-1}$, and the pores are mainly micropores and have a pore volume of $0.118 \text{ cm}^3 \text{ g}^{-1}$. The large specific surface area and pore volume can improve the contact area between the electrode material and electrolyte, as well as provide enough space to mitigate the structural changes during Na^+ insertion/extraction. The electronic state and chemical composition of CoP@NC were further confirmed by XPS. The signals of Co 2p, P 2p, C 1s, and N 1s are shown in Figure 2e, which is consistent with the results of the mapping. Figure 2f is the high-resolution spectrum of Co 2p. The peaks centered at 780.3 eV correspond to Co $2\text{p}_{3/2}$, while the two peaks at 796.3 eV are

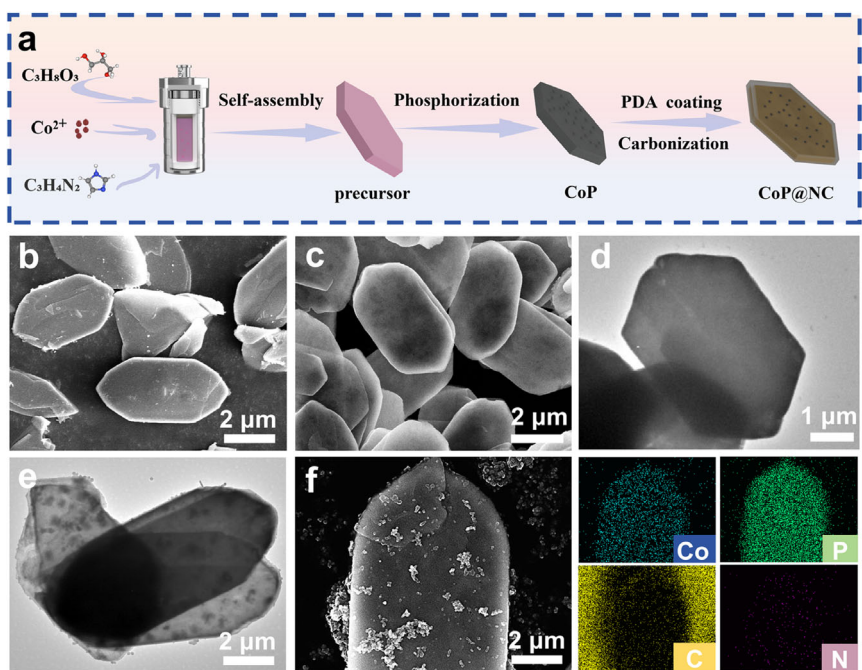


Figure 1. a) Schematic fabrication process of the CoP@NC. b) FESEM image of the precursor. c) FESEM image of the CoP. d) TEM image of the CoP. e) TEM image of the CoP@NC. f) FESEM image and the corresponding elemental mappings of Co, P, N, and C elements (as labeled).

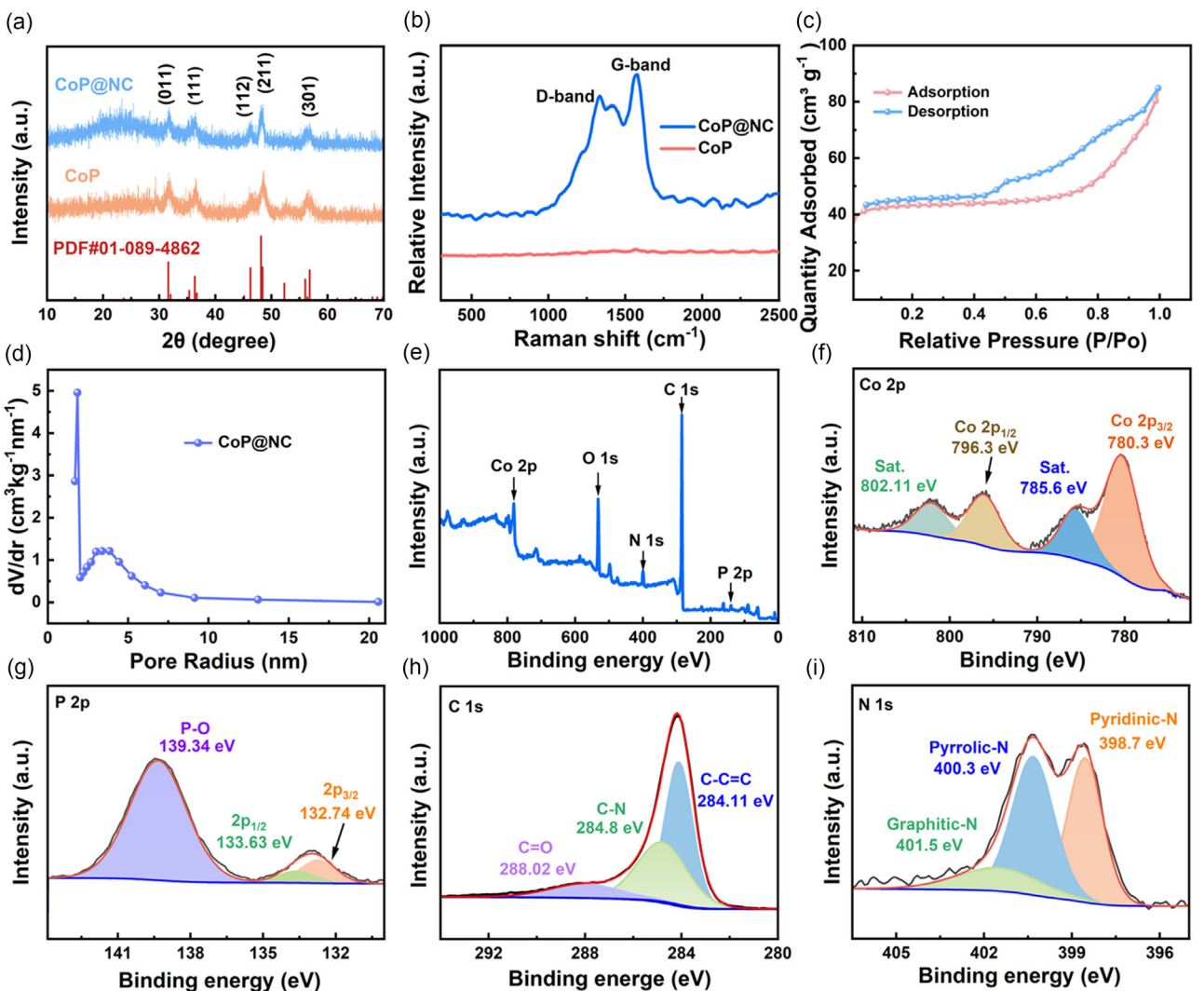


Figure 2. a) XRD patterns of the CoP and CoP@NC. b) Raman spectra of the CoP and CoP@NC samples. c) N_2 physisorption–desorption isotherm of CoP@NC. d) The pore size distribution curve of CoP@NC. e) XPS survey spectrum for CoP@NC; f) High-resolution XPS spectra of Co 2p, g) P 2p, h) C 1s, and i) N 1s.

associated with Co 2p_{1/2}.^[18,19] The peaks at 785.6 and 802.1 eV were assigned to satellite peaks.^[20] The high-resolution P 2p spectrum is shown in Figure 2g. The two peaks located at 132.7 and 133.6 eV correspond to P 2p_{3/2} and P 2p_{1/2} of CoP.^[21] The peak at 139.3 eV can be attributed to oxidized P species, which is due to surface oxidation generated by exposure to air.^[22] Figure 2h shows the high-resolution spectrum of C 1s, with three peaks at 284.1, 284.8, and 288.0 eV assigned to C=C=C, C=N, and C=O bonds, respectively.^[23–25] As shown in Figure 2i, the N 1s band consists of three peaks, which are attributed to pyridinic (398.7 eV), pyrrolic (400.3 eV), and graphitic (401.5 eV) nitrogen atoms, respectively.^[26,27] According to Energy Dispersive Spectrometer testing, the nitrogen content in CoP@NC is 1.73 wt% (Figure S3, Supporting Information).

The electrochemical properties of CoP@NC and CoP were investigated by assembling 2032-type coin cells. Figure 3a and Figure S4a, Supporting Information, show the CV curves of CoP@NC and CoP in the range between 0.01 and 3.0 V vs.

Na^+/Na , respectively. It can be seen that CoP@NC and CoP show similar CV curves, while CoP@NC has a higher curve overlap than CoP, which indicates that CoP@NC has a higher reversibility. In the first discharge curve, the broad reduction peak in the potential range of 0.2–1.1 V and the small peak at 0.05 V can be attributed to the successive conversion of CoP to Co and Na_3 , together with the decomposition of the electrolyte to form the solid electrolyte interphase (SEI) film.^[28] As for the anodic scan, two distinct peaks at 0.07 and 2.06 V are associated with the formation of CoP.^[29] Figure 3b and Figure S4b, Supporting Information, show the galvanostatic charge-discharge (GCD) curves of CoP@NC and CoP at a current density of 0.5 A g^{-1} , respectively. As can be seen from these two Figures, the plateaus in the discharge/charge voltage curves coincide with the position of the redox peak in the CV curve. In addition, the initial discharge and charging capacities of CoP@NC ($375.1/211.9 \text{ mAh g}^{-1}$) are higher than the pure phase CoP ($365.3/170.9 \text{ mAh g}^{-1}$). The initial capacity loss may be caused by some irreversible reactions

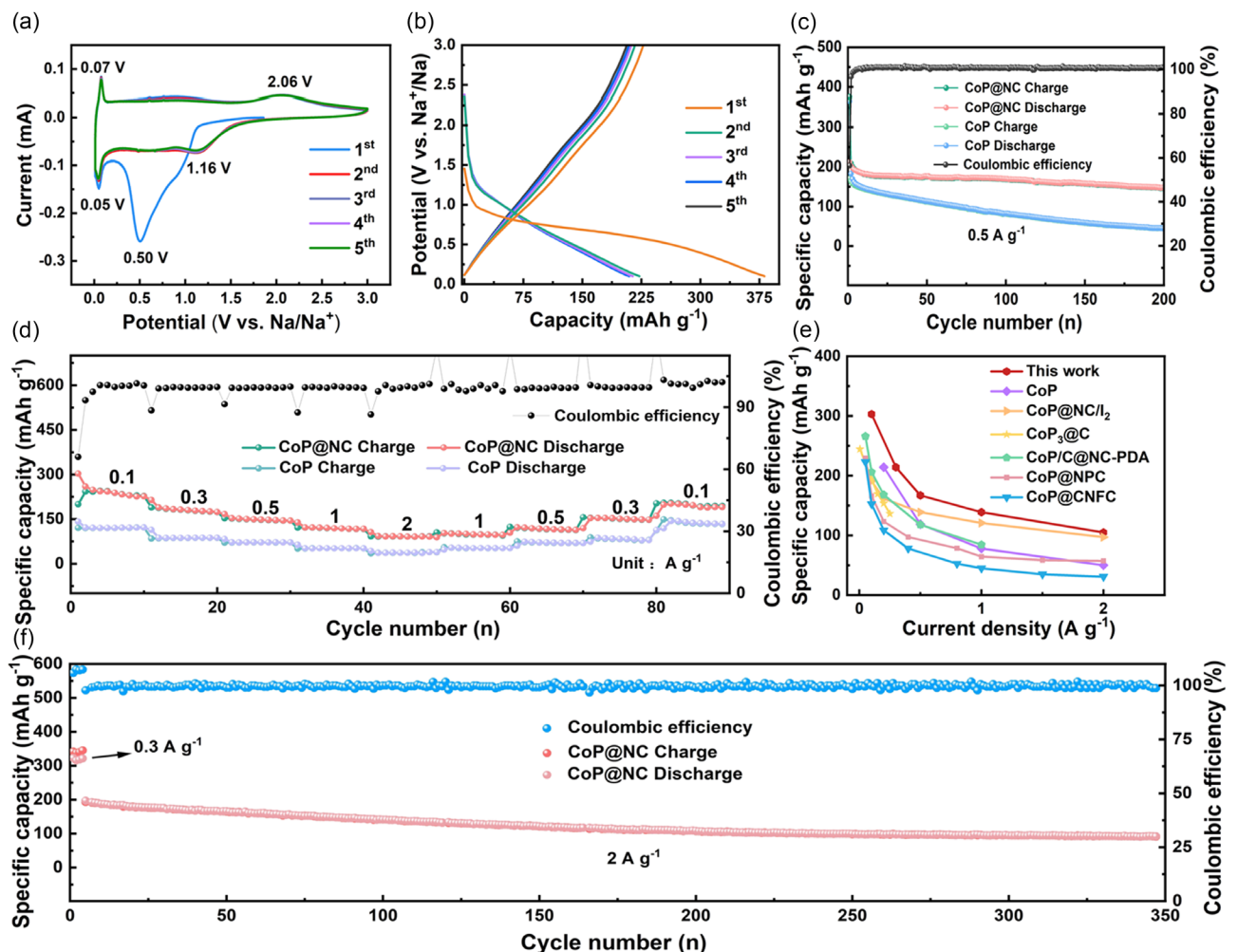


Figure 3. a) CV curves of CoP@NC at a scan rate of 0.1 mV s^{-1} . b) Charge–discharge voltage profiles of CoP@NC at 0.5 A g^{-1} . c) The Cycling performance of CoP@NC and CoP at 0.5 A g^{-1} . d) Rate capability of CoP@NC and CoP at different current densities. e) Comparison with other phosphide anodes of SIBs previously reported in the literature. f) Long-term cycle stability and Coulombic efficiency of CoP@NC at 2 A g^{-1} .

related to the SEI film.^[30] After the first cycle, the GCD curves almost coincide with each other, indicating stable cycling performance for the CoP@NC electrode. After 100 cycles, it still remained at 169.4 mAh g^{-1} (corresponding to a capacity drop of only 0.2% per cycle), higher than the CoP of 81.4 mAh g^{-1} . It is noteworthy that the electrode material still maintains a good integrity after 50 cycles (Figure S5, Supporting Information). Figure 3c shows the cycle performance of CoP@NC and CoP at 0.5 A g^{-1} . The CoP@NC electrode can still maintain a capacity of 146.8 mAh g^{-1} after 200 cycles, which is much higher than that of CoP (44.6 mAh g^{-1}). Impedance measurements are conducted on the electrode materials under open-circuit voltage, after 10 cycles, and after 40 cycles. As shown in Figure S7, Supporting Information, the charge transfer impedance increased slightly after open-circuit voltage and then remained stable, consistent with the relatively stable cycling performance. Figure 3d shows the rate performance of CoP@NC and CoP at different currents from 0.1 to 2 A g^{-1} . We can see that CoP@NC has a much higher reversible capacity than CoP. The reversible capacities of CoP@NC at 0.1 , 0.3 , 0.5 , 1 , and 2 A g^{-1} are 303.3 , 214.3 , 167.2 , 139 , and

106.6 mAh g^{-1} , respectively, and the reversible capacity can also reach 204.9 mAh g^{-1} when the current density is restored to 0.1 A g^{-1} and remains stable for the next cycles, demonstrating the excellent performance of CoP@NC for sodium storage. Compared to previously reported SIBs with transition metal phosphides as anodes, CoP@NC offers significant advantages (Figure 3e).^[31–36] Figure 3f shows the long-cycle performance of CoP@NC at 2 A g^{-1} . It can be seen that CoP@NC shows excellent electrochemical performance, and maintains 92.8 mAh g^{-1} after 350 cycles with a coulombic efficiency close to 100%.

To analyze the reasons for the superior performance of CoP@NC over CoP, we tested the CV curves of the two electrode materials at different sweep speeds. As shown in Figure 4a and Figure 4d, the area enclosed by the CV curves increases with increasing scan rate, and the shapes of all the curves are similar, indicating a clear pseudocapacitive behavior for CoP@NC and CoP as anodes for SIBs during electrochemical reactions. In general, the magnitude of the pseudocapacitance contribution to the total capacity can be qualitatively analyzed according to Equation (1):^[37,38]

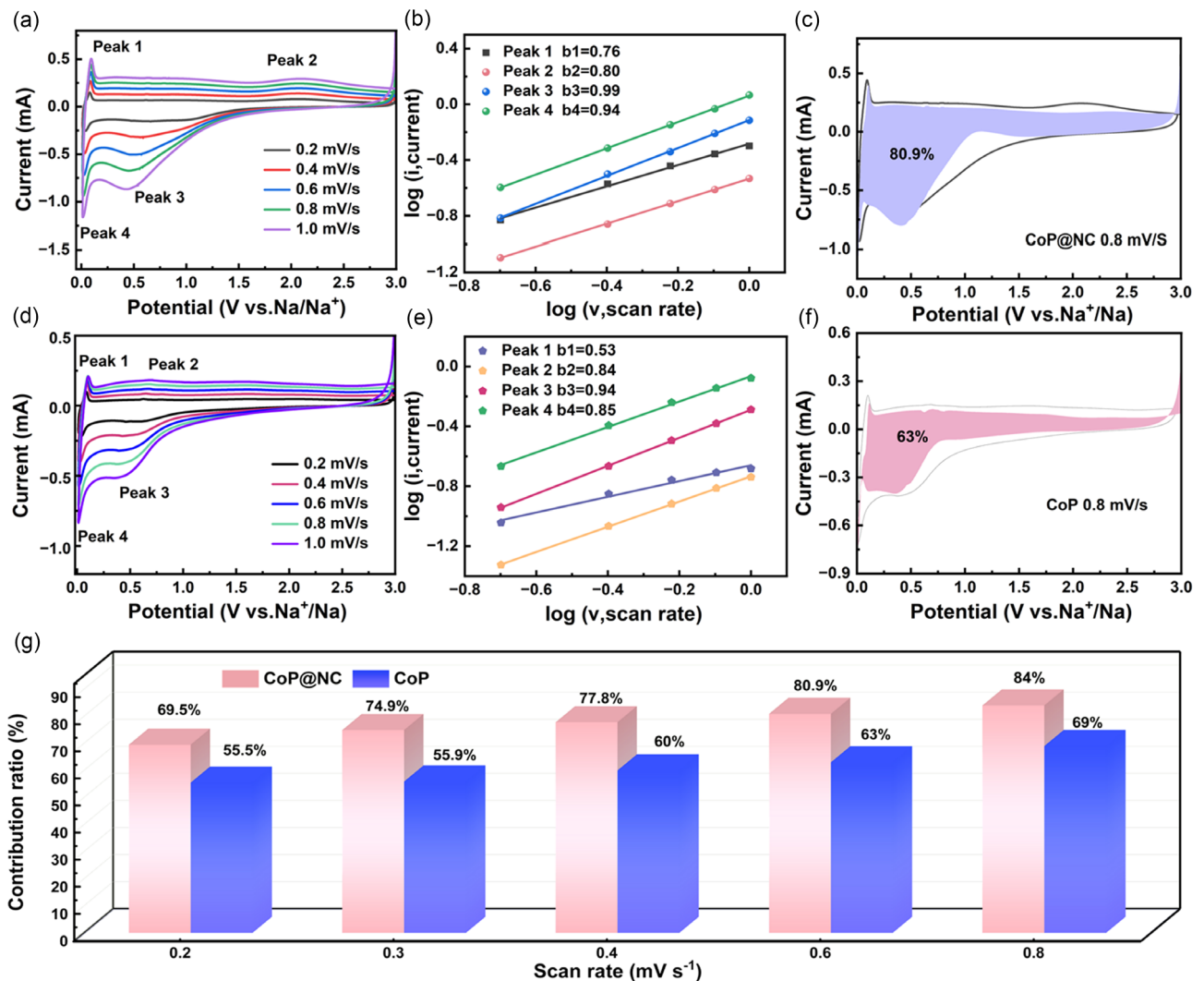


Figure 4. a,d) CV curves of CoP@NC and CoP at different scan rates from 0.2 to 0.8 mV s⁻¹, respectively. b,e) The log (v) versus log (i) plots of at CoP@NC and CoP oxidized and reduced peaks, respectively. c,f) The pseudocapacitive contribution percentage (purple area) of CoP@NC and CoP at 0.8 mV s⁻¹, respectively. g) Contribution ratio of the pseudocapacitive and diffusion-controlled behavior at different scan rates from 0.2 to 0.8 mV s⁻¹.

$$i = a \cdot v^b \quad (1)$$

where b is an important reference for analyzing the sources of contribution to capacity. It can be calculated from the slope of $\log (i)$ and $\log (v)$. In principle, when the b value is equal to 0.5, the electrochemical process is controlled by diffusion, while when $b = 1$, the sodium ion storage process is controlled by pseudocapacitive behavior. Figure 4b,e are the b -value plots of CoP@NC and CoP, respectively. The b -values of CoP@NC at the different redox peaks are greater than pure CoP and close to 1, which indicates a significant pseudocapacitive behavior in CoP@NC. Additionally, Equation (2) can be used to more accurately analyze the diffusion-controlled contribution ($k_2 v^{1/2}$) and the capacitive contribution ($k_1 v$).^[39,40]

$$i(V) = k_1 v + k_2 v^{1/2} \quad (2)$$

According to quantitative analysis, at the scan rate of 0.8 mV s⁻¹, the pseudocapacitance contribution of CoP@NC is

80.9% (Figure 4c), which is higher than that of CoP (63%, Figure 4f). In addition, Figure 4g shows histograms of the pseudocapacitance contribution of CoP@NC and CoP at different scan rates. We can see that the contribution of pseudocapacitance rises with increasing sweep speed, and the contribution of pseudocapacitance of CoP@NC is higher than that of CoP. Thus, improvements in the electrochemical performance of CoP@NC, particularly in rate capability, are associated with an increased contribution from pseudocapacitive behavior.

In order to determine the ion diffusion coefficients of the two electrode materials, we further tested the GITT curves for the seventh cycle, as shown in Figure 5a,d, respectively. In the GITT test, the battery is charged or discharged at 50 mA g⁻¹ for 20 min, followed by an open circuit step for 60 min to relax to equilibrium and repeat the process until the charging (or discharging) voltage reaches 3 V (0.01 V). Figure 5b,e show a single GITT titration curve during charging. Where $\Delta\epsilon_s$ is the voltage variation in two consecutive relaxation periods; $\Delta\epsilon_t$ is the voltage variation during the

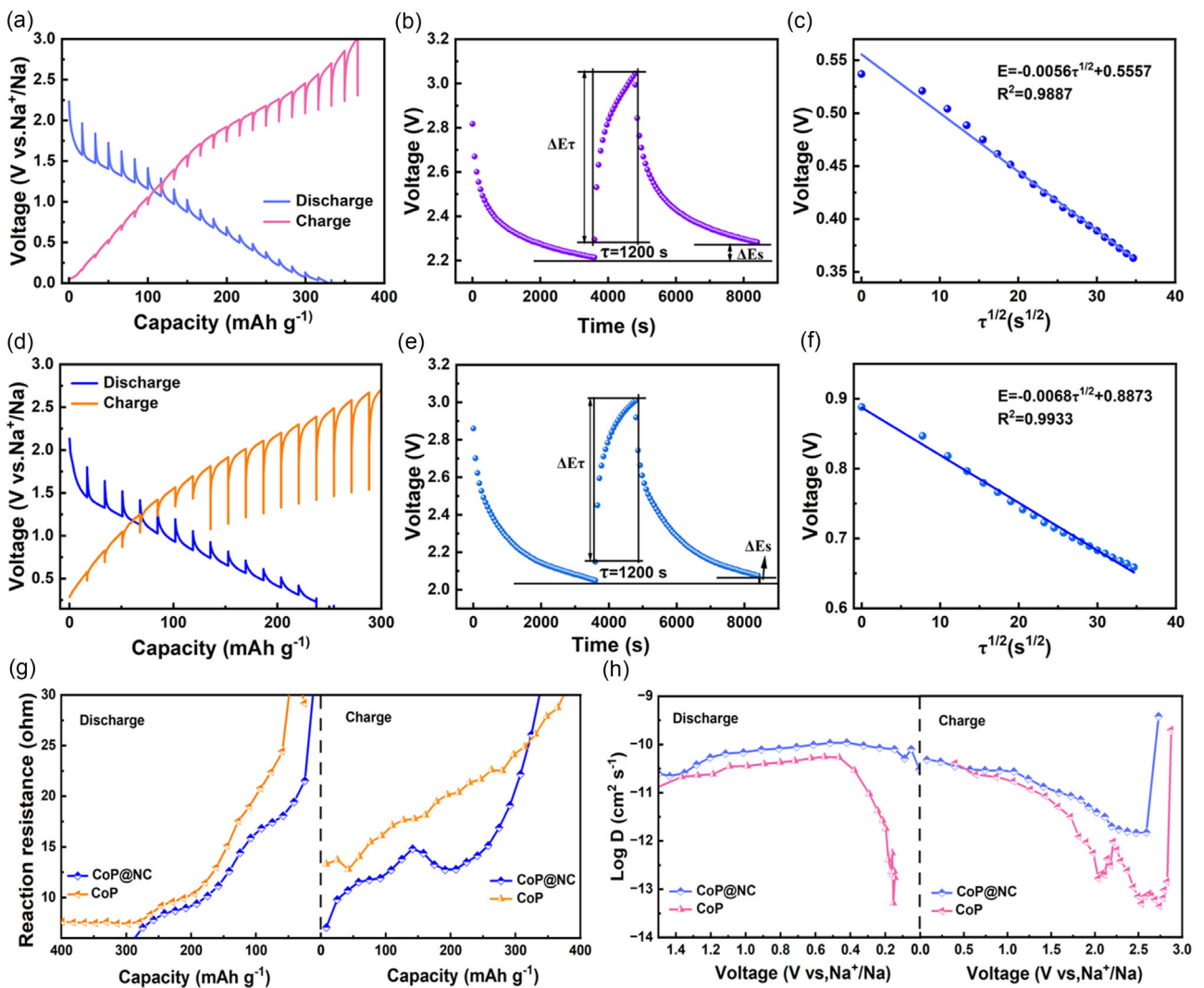


Figure 5. a,d) GITT voltage profiles of CoP@NC and CoP during the seventh cycle, respectively. b,e) A single GITT titration curve of CoP@NC and CoP during the charge process, respectively. c,f) The plots of voltage vs. root of pulse time ($\tau^{1/2}$). g) Comparison of electric resistance for CoP@NC and CoP during discharge and charge. h) Comparison of D_{Na^+} for CoP@NC and CoP during discharge and charge.

constant current pulse. Fick's second law was used to calculate the diffusion coefficients of the two electrode materials, as shown in Figure 5c,f. voltage vs $\tau^{1/2}$ fitted a linear relationship, so Equation (3) was used to quantify the chemical diffusion coefficient of Na^+ (D_{Na^+}) in the electrode material.^[41,42]

$$D_{\text{Na}^+} = \frac{4}{\pi} \left(\frac{m_B y_m}{M_B S} \right)^2 \left(\frac{\Delta E_s}{dE_r/d\sqrt{\tau}} \right)^2 \quad (3)$$

As can be seen in Figure 5g, CoP@NC shows lower reaction resistance than pure CoP during discharge and charging, indicating that CoP@NC has a higher chemical diffusion coefficient. Figure 5h shows the relationship between D value and voltage during discharging and charging, respectively. It can be seen that CoP@NC has a higher D-value, which means that the NC coated on the outside of the CoP nanosheets effectively improves the reaction kinetics. This is consistent with the impedance results (Figure S6, Supporting Information).^[43] Based on the excellent

cycling performance and reaction kinetics of CoP@NC, a full cell is assembled using $\text{Na}_3\text{V}_2(\text{PO}_4)_3$ as the cathode. Based on the GCD curves of the half cells using CoP@NC and $\text{Na}_3\text{V}_2(\text{PO}_4)_3$ electrode materials (Figure S8a, Supporting Information), the voltage window for the full cell is selected as 0.5–3.5 V. The GCD curve of the full cell at 0.5 A g^{-1} is shown in Figure S8b, Supporting Information, demonstrating an initial charge capacity of 317.5 mAh g^{-1} with good cycling stability. After 50 cycles, the capacity remains at 134.9 mAh g^{-1} (Figure S8c, Supporting Information).

3. Conclusion

In summary, nitrogen-doped carbon-coated CoP nanosheets (CoP@NC) were precisely synthesized by a simple strategy. Benefiting from the encapsulation of the nitrogen-doped carbon layer, CoP@NC exhibits superior properties compared to CoP. It

maintains a high reversible capacity of 147 mAh g^{-1} after 200 cycles at 0.5 A g^{-1} . It also shows superior rate capability for Na-ion storage. The increased contribution of pseudocapacitance and the improved reaction kinetics are important reasons for the superior performance of CoP@NC over pure CoP. It is expected that this strategy may provide a new method for other transition metal phosphides applied as anodes for Na-ion batteries. This strategy may provide insights into the performance enhancement of other transition metal phosphides as Na-ion battery anodes.

4. Experimental Section

Synthesis of Precursor

The precursor was synthesized by the solvothermal method. Firstly, 0.33 mmol $\text{Co}(\text{NO}_3)_2 \cdot 6\text{H}_2\text{O}$ (Ronne Reagent, AR, 99%), and 0.76 mmol imidazole (mIn, Macklin Chemical Reagents Co., Ltd., AR, 99%) were dispersed into 10 mL glycerol (Gly, Sinopharm Chemical Reagent Co., Ltd., AR, 99%) via continued vigorous stirring. The dispersion was then transferred to a Teflon-lined stainless steel autoclave and placed in an oven for 12 h at 160°C . After cooling to room temperature, the dispersion was collected by filtration and washed several times with ethanol, yielding 13.34 mg of pink precursor powder.

Synthesis of CoP

Two porcelain boats containing the precursors and NaH_2PO_2 were placed in the furnace in a 1:10 weight ratio, while the precursor was placed downstream. Then heated to 350°C at a heating rate of 3°C min^{-1} under an Ar atmosphere and kept for 2 h to obtain CoP.

Synthesis of CoP@NC

First, 0.1 g of CoP powder was dispersed into a 0.1 mol L^{-1} Tris-HCl solution and stirred for 20 minutes. Then, 80 mg of dopamine hydrochloride was added and stirred continuously for six hours to obtain a black CoP@PDA powder. Finally, CoP@NC was obtained by carbonization of CoP@PDA at 550°C .

Materials Characterization

The CoP@NC and CoP microstructures were characterized using field-emission scanning electron microscopy (FESEM, Zeiss GeminiSEM 300, Germany) and transmission electron microscopy (TEM, JEOL-1400 Plus, Japan). The crystalline phases of CoP@NC and CoP were determined by powder X-ray diffraction (XRD-7000, Shimadzu, Japan) using a Cu K α source. The nitrogen adsorption-desorption isotherm and pore size distribution of CoP@NC were obtained by the Brunauer-Emmett-Teller method (BET, Micromeritics ASAP 2020, USA). The chemical composition and bonding state of CoP@NC were tested by X-ray photoelectron spectroscopy (XPS, ESCALAB 250Xi, USA).

Electrochemical Measurements

CoP@NC, Super P, and polyvinylidene fluoride (PVDF) were mixed and milled according to a mass ratio of 7:2:1, and appropriate amounts of N-methylpyrrolidone (NMP) were added dropwise to

make a slurry and transferred to the copper foil. After the coated electrodes were dried, they are cut into round electrodes with a diameter of 12 mm using a slicer, and each electrode was loaded with $1.05\text{--}1.3 \text{ mg cm}^{-2}$ of active material. The battery was assembled using a CR2032 battery cell shell in an argon-filled glove box. The counter electrode was a sodium sheet with a diameter of 14 mm. Glass fiber was used as the separator. The electrolyte used was 1 M NaPF_6 dissolved in diethyleneglycol dimethyl ether. CV was tested on a CHI 760E electrochemical workstation with a voltage range of 0.01–3 V. The galvanostatic charge/discharge tests were performed using the Wuhan Blue Power Test System.

Acknowledgements

This work was supported by the National Natural Science Foundation of China (no. 22305210, and 52371238), Yantai University Laboratory Open Fund. Shandong (Yantai) Sino-Japan Industrial Technology Research Institute (Yantai Industrial Technology Research Institute) for open projects (KXDNY2024-6).

Conflict of Interest

The authors declare no conflict of interest.

Author Contributions

The manuscript was written through the contributions of all the authors. All the authors have given approval to the final version of the manuscript. Jingyu Guo and Qingzhe Meng contributed equally to this work.

Data Availability Statement

The data that support the findings of this study are available from the corresponding author upon reasonable request.

Keywords: anode material · CoP · nanosheets · nitrogen-doped carbon · sodium-ion batteries

- [1] Y. Jiang, Z. Zhang, H. Liao, Y. Zheng, X. Fu, J. Lu, S. Cheng, Y. Gao, *ACS Nano* **2024**, *18*, 7796.
- [2] J. Li, Y. He, Y. Dai, H. Zhang, Y. Zhang, S. Gu, X. Wang, T. Gao, G. Zhou, L. Xu, *Adv. Funct. Mater.* **2024**, *34*, 2406915.
- [3] Y. Wu, X. Xu, S. Shi, F. Li, S. Ji, J. Zhao, J. Liu, Y. Huo, *Chin. Chem. Lett.* **2025**, *36*, 110062.
- [4] C. Dong, C. Li, Y. Zhang, Q. Dong, K. Li, Y. Wang, F. Jiang, N. Wang, S. X. Dou, Z. Bai, *Chem. Eng. J.* **2025**, *514*, 163349.
- [5] L. Yu, Z. Li, W. Cai, H. Xie, J. Wang, Y. Ling, F. Huang, H. Li, G. Zhu, H. Jin, S. Wang, *Small* **2024**, *20*, 2404059.
- [6] S. Li, J. Zhang, Y. Li, P. Fan, M. Wu, *Nano Res. Energy* **2024**, *3*, e9120098.
- [7] Y. Li, S. Liu, W. Sun, R. Lu, C. Liu, Q. Sun, *New J. Chem.* **2024**, *48*, 6633.
- [8] Y. Zhou, Y. Wang, Y. Zhang, Z. Bai, M. Y. Wang, Y. Zhai, W. Du, Z. Yan, S. X. Dou, N. Wang, F. Jiang, C. Dong, *Carbon Energy* **2025**, *7*, e721.
- [9] Y. Wang, X. Zhang, M. Zhou, J. Huang, *Nano Res. Energy* **2023**, *2*, e9120046.
- [10] H. Liu, F. Liu, Z. Qu, J. Chen, H. Liu, Y. Tan, J. Guo, Y. Yan, S. Zhao, X. Zhao, X. Nie, X. Ma, Z. Pei, M. Liu, *Nano Res. Energy* **2023**, *2*, e9120049.

- [11] C. Shi, D. Muhtar, X. Lu, F. Liu, X. Lu, Z. Sun, Z. Guo, *Adv. Energy Mater.* **2025**, *15*, 2500448.
- [12] X. Nie, Z. Chen, B. Deng, L. Shao, J. Xu, X. Shi, Z. Sun, *Adv. Energy Mater.* **2025**, *15*, 2500069.
- [13] Y. Yun, B. Xi, F. Tian, W. Chen, W. Sun, H. Pan, J. Feng, Y. Qian, S. Xiong, *Adv. Energy Mater.* **2021**, *12*, 2103341.
- [14] Y. Ran, C. Xu, D. Ji, H. Zhao, L. Li, Y. Lei, *Nano Res. Energy* **2024**, *3*, e9120092.
- [15] S. Liu, Q. Shi, X. Liu, J. Fan, L. Ren, J. Tong, *Chem. Eng. J.* **2024**, *502*, 157889.
- [16] J. Zhu, Q. He, Y. Liu, J. Key, S. Nie, M. Wu, P. K. Shen, *J. Mater. Chem. A* **2019**, *7*, 16999.
- [17] Z. Zhao, H. Li, Z. Yang, S. Hao, X. Wang, Y. Wu, *J. Alloy. Compd.* **2020**, *817*, 152751.
- [18] S. Liu, Q. Shi, X. Liu, M. Zhang, F. Lin, J. Tong, *J. Energy Storage* **2025**, *126*, 117026.
- [19] Q. Chang, Y. Jin, M. Jia, Q. Yuan, C. Zhao, M. Jia, *J. Colloid Interface Sci.* **2020**, *575*, 61.
- [20] L. Zeng, Y. Fang, L. Xu, C. Zheng, M.-Q. Yang, J. He, H. Xue, Q. Qian, M. Wei, Q. Chen, *Nanoscale* **2019**, *11*, 6766.
- [21] Z. Chen, T. Tao, C. Shi, X. Shi, L. Shao, J. Xu, Z. Sun, *Carbon Neutraliz.* **2025**, *4*, e70010.
- [22] R. He, X. Wang, J. Li, L. Chang, H. Wang, P. Nie, *Appl. Surf. Sci.* **2024**, *654*, 159532.
- [23] Y. Zhang, J. Guo, X. Liu, Y. Gao, Z. Bai, N. Wang, Y. Wang, F. Jiang, Y. Zhai, S. X. Dou, C. Dong, *Adv. Funct. Mater.* **2025**, *35*, 2504553.
- [24] H. Li, Y. He, Q. Wang, S. Gu, L. Wang, J. Yu, G. Zhou, L. Xu, *Adv. Energy Mater.* **2023**, *13*, 2302901.
- [25] F. Kong, Y. Ge, S. Tao, Z. Yuan, C. Lu, Z. Han, L. Yu, B. Qian, *Chin. Chem. Lett.* **2024**, *35*, 108552.
- [26] B. Wang, L. Wang, D. Ding, Y. Zhai, F. Wang, Z. Jing, X. Yang, Y. Kong, Y. Qian, L. Xu, *Adv. Mater.* **2022**, *34*, 2204403.
- [27] C. Dong, H. Shao, Y. Zhou, W. Du, L. Li, J. Sun, Z. Yan, Z. Hu, S. Chou, F. Jiang, *Adv. Funct. Mater.* **2023**, *33*, 2211864.
- [28] Z. Gu, J. Li, P. Song, Y. Wang, J. Yang, T. Wang, C. Wang, *J. Materomics* **2023**, *9*, 1185.
- [29] J. Zhang, K. Zhang, J. Yang, G. H. Lee, J. Shin, V. W.-H. Lau, Y. M. Kang, *Adv. Energy Mater.* **2018**, *8*, 1800283.
- [30] S. Liu, Z. Qin, J. Guo, S. Guo, Z. Zhou, Q. Shi, Y. Zhang, Z. Geng, *J. Energy Storage* **2024**, *98*, 113131.
- [31] M. Gu, S. Chen, J. Xu, X. Shi, L. Shao, Z. Sun, *ACS Appl. Mater. Interfaces* **2025**, *17*, 22546.
- [32] L. Zhu, X. Guan, Z. Zhang, Y. Fu, Z. Yuan, C. Zhang, Y. Wang, H. Fan, H. Xu, X. Li, H. Li, B. Jia, H. Yu, Y. Sun, T. Ma, *Chem. Commun.* **2025**, *61*, 961.
- [33] W. Zhao, X. Ma, G. Wang, X. Long, Y. Li, W. Zhang, P. Zhang, *Appl. Surf. Sci.* **2018**, *445*, 167.
- [34] B. Wang, L. Yang, F. Yuan, D. Zhang, H. Wang, J. Wang, Q. Wang, Z. Li, *J. Alloy Compd.* **2022**, *925*, 166679.
- [35] Y. Wang, J. Liu, X. Chen, B. Kang, H.-E. Wang, P. Xiong, Q. Chen, M. Wei, N. Li, Q. Qian, L. Zeng, *Carbon* **2022**, *189*, 46.
- [36] J. Xu, F. Xie, L. Huang, N. Li, S. Peng, W. Ma, K. Zhang, Y. Wu, L. Shao, X. Shi, J. Chen, L. Tao, K. Zhang, Z. Zhang, Y. Wang, Z. Sun, *Nat. Commun.* **2025**, *16*, 4977.
- [37] Y. Wang, Y. Wang, Z. Cai, Z. Yu, H. Dong, Y. Zhang, Y. Zhou, X. Zhang, Y. Zhai, F. Jiang, C. Dong, *Inorg. Chem. Front.* **2024**, *11*, 7552.
- [38] L. Wang, Z. Kong, M. Muhammad, B. Wang, F. Wang, Z. Jing, G. Qu, X. Yang, J. Feng, J. Dou, Y. Kong, L. Xu, *Adv. Funct. Mater.* **2025**, *35*, 2423524.
- [39] Y. Du, Y. Wang, Z. Cao, J. Ding, Z. Guo, H. Shao, Y. Li, J. Yan, R. Sun, X. Zhang, T. Sun, F. Jiang, C. Dong, *Mater. Today Chem.* **2024**, *35*, 101838.
- [40] C. Yi, L. Chen, C. Ping, R. Zhang, C. Dong, Y. Huang, M. Wang, Y. Zhang, *J. Energy Storage* **2024**, *100*, 113716.
- [41] Z. Jing, M. Mamoor, L. Kong, L. Wang, B. Wang, M. Chen, F. Wang, G. Qu, Y. Kong, D. Wang, X. He, C. Wang, X. Zhang, Y. Zhang, G. Wang, L. Xu, *Angew. Chem. Int. Ed.* **2025**, *64*, e202423356.
- [42] C. Dong, L. Wu, Y. He, Y. Zhou, X. Sun, W. Du, X. Sun, L. Xu, F. Jiang, *Small* **2020**, *16*, 2004580.
- [43] B. Cheng, Y. He, C. Li, H. Liu, B. Sun, S. Gu, G. Zhou, Z. Tong, N. Wang, G. Wang, Z. Bai, *Adv. Funct. Mater.* **2025**, *e16499*, <https://doi.org/10.1002/adfm.202516499>.

 Manuscript received: August 16, 2025

Revised manuscript received: October 1, 2025

Version of record online: